ACS APPLIED MATERIALS & INTERFACES

Research Article

www.acsami.org

Multivalent Glycosylation of Fluorescent Gold Nanoclusters Promotes Increased Human Dendritic Cell Targeting via Multiple Endocytic Pathways

Xavier Le Guével,[*,†] Monica Perez Perrino,[‡] Tahia D. Fernández,[§,∥] Francisca Palomares,[§,∥] Maria-José Torres,[∥] Miguel Blanca,[∥] Javier Rojo,[‡] and Cristobalina Mayorga[§,∥]

[†]Therapeutic Nanosystems, The Andalusian Centre for Nanomedicine and Biotechnology (BIONAND), 29590 Málaga, Spain
[‡]Glycosystems Laboratory, Instituto de Investigaciones Químicas (IIQ), CSIC−University of Seville, 41092 Seville, Spain
[§]Research Laboratory and [∥]Allergy Service, IBIMA, Regional University Hospital of Málaga, UMA, 29010 Málaga, Spain

Supporting Information

ABSTRACT: We report the synthesis and characterization of gold nanoclusters (Au NCs) stabilized by a mixture of zwitterionic and multivalent mannose ligands. Characterization of this carbohydrated nanosystem confirms its small size (~2 nm), intense red−NIR fluorescence, relatively high affinity to lectin (ConA), and stability in physiological media. Cell studies performed using human-monocyte-derived dendritic cells (DCs) show that Au NC uptake efficiency is greatly enhanced by the presence of surface carbohydrate (>250% compared to noncarbohydrated Au NCs), allowing their detection in cells by fluorescence following incubation with concentrations as low as 1 μg mL^{-1}. Investigation using electron microscopy and pharmacological inhibitors indicates that Au NC uptake is mediated by multiple endocytic pathways involving the engulfment of Au NCs into endosomes and partial transport to lysosomes. Results show that clathrin- and F-actin-dependent pathways play major roles in Au NC uptake by DCs, regardless of whether or not they are coated with carbohydrates. In contrast, a specific C-lectin inhibitor induces a 60% decrease in DC particle uptake only for the carbohydrate-coated Au NCs. This study demonstrates that the combination of ultrasmall gold NCs and functionalization with multivalent mannose ligands results in greatly enhanced human DC targeting, presumably due to increased diffusion and target cell binding, respectively.

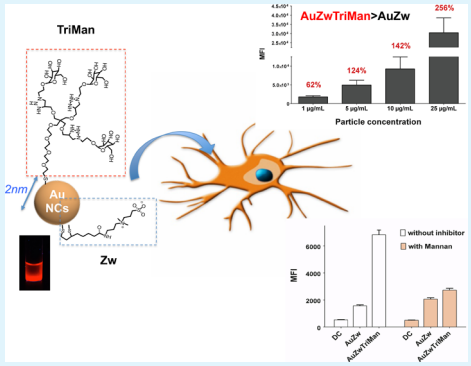

KEYWORDS: *gold nanoclusters, mannose, targeting, cell uptake, dendritic cells*

INTRODUCTION

As part of the development of nanoparticle (NP) vaccines for the treatment of cancer, infectious diseases, and allergies, many efforts have focused on dendritic cell (DC) targeting.[1−3] DCs are one of the most potent types of antigen-presenting cell (APC) and are seen as key players in the initiation and control of adaptive immune responses.[4,5] Furthermore, DCs reside in the periphery and in lymphoid organs, which makes them ideal sentinels for pathogen recognition. As a consequence, a new generation of particulate-based vaccines are designed (i) to target DCs in specific tissues and (ii) to deliver efficiently antigens to DCs to either stimulate the immune response for immunotherapy or downregulate it for the treatment of allergic diseases or organ transplantation.[6−8]

One of the main potential advantages of using NPs for vaccines is based on their capacity to stabilize vaccine antigens while simultaneously acting as an adjuvant.[6,9,10] Antigens can be encapsulated or conjugated to the NP surface, with both methods offering distinct advantages. For instance, the loading of allergens inside NPs is an elegant strategy to protect the therapeutic agent from clearance at the injection site,[11] while surface conjugation enhances immune cell antigen presentation.[12] In addition, NPs are attractive for clinical and biological applications due to their low immunogenicity, low toxicity, and good biocompatibility.[9] In other words, NPs have the potential, at least in theory, to deliver antigens efficiently to DCs by different pathways due to our ability to functionalize their surface with biomolecules and their capacity to modulate the immune response. Extensive research has focused on a plethora of biodegradable [poly(lactic-*co*-glycolic acid), dendrimers, chitosan, viruslike particles, liposomes)[1,13−15] and nondegradable (gold, silicon, polystyrene)[16−18] NPs designed to reach DCs in in vitro and in vivo models. Two major NP parameters are considered crucial for efficient DC targeting: (1) NP size and (2) NP surface functionalization. Size has been shown to drastically influence particle recognition by the immune system, where particles bigger than 1 μm are rapidly phagocytized by macrophages.[6] Studies performed with in vivo models have

Received: July 19, 2015
Accepted: September 2, 2015
Published: September 2, 2015

DOI: 10.1021/acsami.5b06541
ACS Appl. Mater. Interfaces 2015, 7, 20945−20956

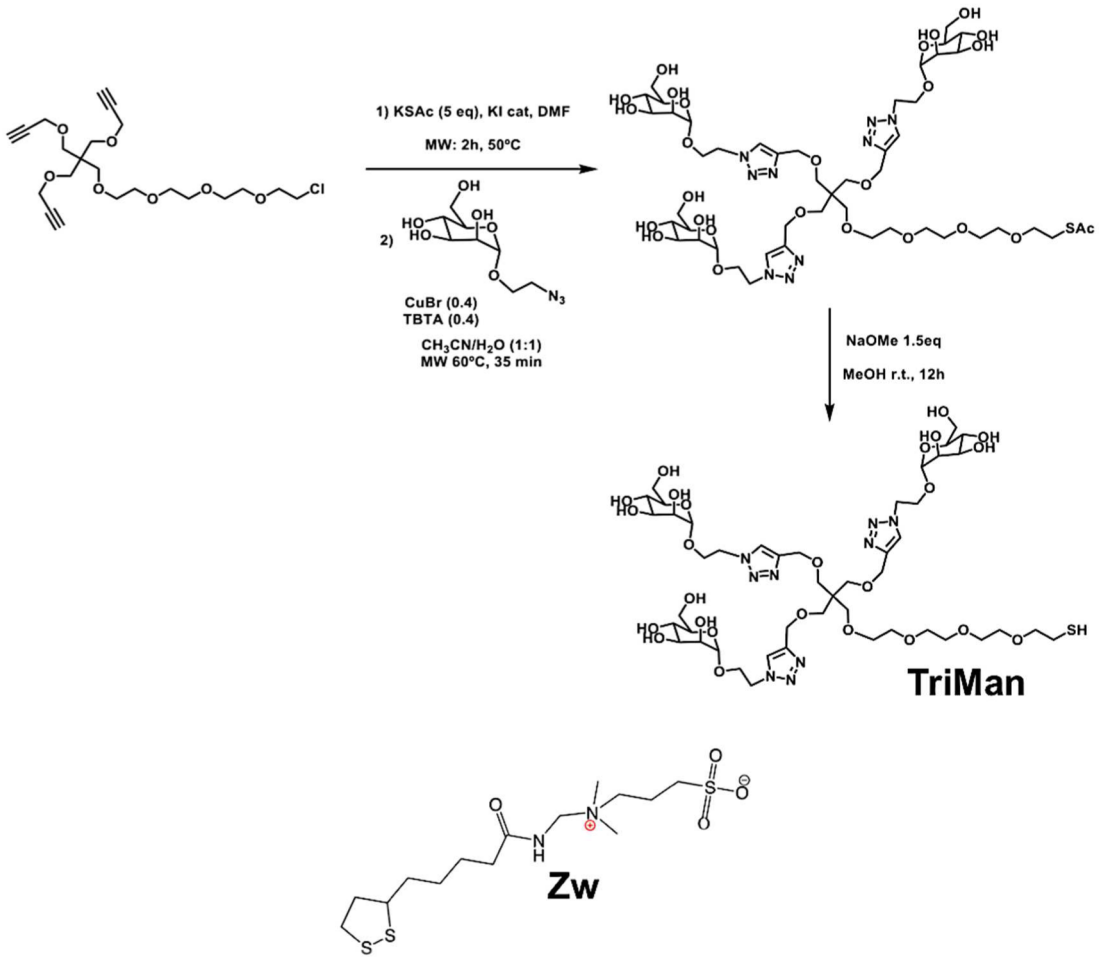

Figure 1. Synthetic steps for the preparation of the trivalent mannose compound (TriMan) and the chemical formula of the thioctic zwitterion compound (Zw).

demonstrated that NPs enter lymphatic capillaries and are taken up by peripheral DCs close to the injection site, with higher uptake efficiency for particles in the range of 20−200 nm.[11,19] Therefore, smaller NPs might reach a higher number of DCs due to their greater diffusion and penetration. However, determining the relative effectiveness of narrower NP size ranges has been the subject of contradictory results in in vitro and in vivo models, revealing the complexity of the different factors involved in NP uptake.[20] Numerous independent studies have shown that the physicochemical parameters of NPs have a direct impact on passive DC targeting,[18,21] while the presence of functional surface groups, such as carbohydrates or antibodies, have been shown to specifically bind DC surface receptors.[22] This strategy has been remarkably successful, notably by targeting C-lectin receptors (CLRs) using customized carbohydrate ligands. The mannose receptor (MR) and DC-SIGN are the most important and best characterized CLRs present on the surface of DCs.[23] Carbohydrate synthesis, the DC targeting efficiency of carbohydrate-coated NPs, and their biological applications have been covered by several excellent reviews.[2,24] One elegant approach to enhance CLR targeting involves taking advantage of the multivalency of carbohydrate compounds. For example, Rojo and co-workers designed different glycosystems based on the attachment of multivalent mannoses or fucoses to nanocarriers (dendrimers,[25] fullerenes[26]) and demonstrated their high uptake efficiency by targeting DC-SIGN receptors. They also showed how these multivalent "glyconanosystems" could be applied to inhibit viral infections such as HIV[27] and the Ebola virus with very high efficiency and selectivity.[26,28,29]

Metal (Au, Ag, Pt, Cu) nanoclusters (NCs) are a family of particles composed from just a handful of atoms, up to ∼100 atoms, thus spanning the gap between individual atom and nanoparticle properties. NCs exhibit unique optoelectronic properties due to their strong quantum confinement in this size regime (∼0.5 nm for Au and Ag).[30,31] Recently, numerous Au and Ag NCs have been reported that exhibit intense luminescence in a broad spectral range stretching from UV to near-infrared (NIR).[31] Such nanostructures require stabilizing agents, or templates, to maintain their stability in solution and prevent the loss of their unique optical properties. Commonly reported templates for Au and Ag NCs include dendrimers,[32] biomolecules (DNA, proteins, peptides, etc.),[33] and thiolated molecules.[34] In the latter example, extensive experimental studies supported by theoretical models[30,35] demonstrate that both the NC core and the thiolated gold(I) shell contribute to their photoluminescence properties, with the shell being especially important for red−NIR region emissions.[36−39] For instance, the Mattoussi lab reported the preparation of red-emitting Au NCs with a quantum yield of up to 14% when stabilized with bidentate thiolated ligands containing a zwitterionic group.[40] NC features such as tunable photoluminescence,[41,42] multiexponential fluorescence lifetime,[43,44] or aggregation-induced enhancement[45] have been extensively

DOI: 10.1021/acsami.5b06541
ACS Appl. Mater. Interfaces 2015, 7, 20945−20956

studied with potential applications in the fields of sensing,[46] bioimaging,[47] and optics.[48] Other interesting properties of NCs relevant for therapeutic applications rely on their ultrasmall size, low toxicity, and stability in physiological media. In vitro studies in mice have demonstrated the rapid and efficient clearance of glutathione-stabilized Au NCs due to their size being smaller than the kidney filtration threshold ($\phi \sim 5.5$ nm).[49,50] NCs have shown also promising results for cancer therapy[49,51] and vaccine development.[52] For example, we have recently shown how their small size and the use of a zwitterionic ligand promote their uptake by monocyte-derived DCs and induce a strong immunosuppressive effect,[52] which we believe to be related to the dual action of the high diffusion of the particle in solution and the ligand contribution.

In the present study, we decided to combine the ultrasmall size of Au NCs (~2 nm) and the multivalency of a mannose ligand in the presence of monocyte-derived DCs. Our aim was to determine the uptake efficiency of this nanosystem and study the mechanism by which Au NCs protected by zwitterionic or a mixture of zwitterionic and carbohydrate (i.e., trivalent mannose) ligands are uptaken (Figure 1). After comprehensively characterizing the chemical and optical properties of multivalent mannose-stabilized Au NCs, cell studies determined a strong increase in DC uptake efficiency due to the presence of the multivalent mannose ligand. Electron microscopy data indicate that Au NC uptake in DCs occurs via endocytic pathways with particle accumulation visible in endosomes and lysosomes. Results from experiments using pharmacological inhibitors of different cellular pathways confirm the endocytic uptake of Au NCs by multiple pathways with a strong contribution from clathrin- and F-actin-dependent mechanisms. The specific uptake of multivalent mannose-stabilized Au NCs by C-lectin receptors was also clearly demonstrated by a 60% decrease in the presence of mannan, a specific carbohydrate inhibitor.

MATERIALS AND METHODS

All chemical products were purchased from Sigma-Aldrich. Ultrapure Milli-Q water was used for all syntheses.

Synthesis of the Ligands. Thioctic zwitterion (Zw, $M \sim 412$ g mol^{-1}) was synthesized following the protocol described elsewhere.[40,53] Synthesis of the dithiol trivalent mannose linker ($M \sim 2377$ g mol^{-1}) corresponding to two monomers, here called TriMan ($M \sim 1190$ g mol^{-1}), is reported in the Supporting Information (SI) (refer to Figures S1 and S2 for details of the synthesis and characterization by NMR, FTIR, and mass spectroscopy).

Synthesis of Au NCs. Zw-ligand-stabilized Au NCs were prepared by adding gold salt ($HAuCl_4 \cdot 3H_2O$, 50 mM) to a basic solution (pH 10) containing the ligand in the presence of $NaBH_4$ reducing agent (50 mM) and stirring for 15 h. Zwitterion-stabilized Au NCs (AuZw) were synthesized with a 1:10:2 Au:Zw:$NaBH_4$ molar ratio. The second type of NC containing the TriMan coligand (AuZwTriMan) was prepared using the same protocol as used for AuZw plus the dropwise addition of a specific amount of dithio-TriMan 10 min after the addition of $NaBH_4$. The optimum molar ratio for AuZwTriMan is Au:Zw:$NaBH_4$:TriMan = 1:10:2:0.21. Solutions were then dialyzed with a 3.5 kDa cutoff membrane (SnakeSkin, ThermoScientific) for 24 h to remove excess free ligands and then concentrated to 500 μg gold/mL with Amicon 3 kDa cutoff filters (13 600 rpm, 20 min) in water and kept refrigerated until use.

NC Characterization. NMR spectroscopy of AuZw, AuZwTriMan, and the free ligands (Zw, TriMan) was performed using a Bruker Ascend 400 MHz NMR with deuterium oxide. Freeze-dried samples were characterized by infrared spectroscopy using a JASCO FTIR-4100 from 650 to 4000 cm^{-1}.

PAGE electrophoresis of the NCs, AuZw, and AuZwTriMan on a 15% polyacrylamide gel was carried out using the Bio-Rad mini-Protean system (Hercules, CA) at 100 V for 120 min. Each well was loaded with 20 μL of concentrated sample mixed with 10 μL of glycerol. The molecular weight was determined with a Precision Plus Protein Dual Xtra standard indicator (2–250 kDa).

The presence of fragmented gold NCs and TriMan ligand mass were determined by matrix-assisted laser desorption/ionization (MALDI) on a 4700 Proteomics Analyzer mass spectrometer (ABSCIEX, Framingham, MA). Samples were prepared with the matrix of α-cyano-4-hydroxycinnamic acid (CHCA), 5 mg/mL in 50% acetonitrile, 0.1% trifluoroacetic acid (TFA) with a 1:1 volume ratio. The samples were analyzed in reflective mode and linear middle mass positive ion mode, with 20 kV source 1 acceleration voltage. The grid 1 voltage was set to 92.5% of the source 1 acceleration voltage. Delay time DE1 was 850 ns, and the low mass gate was enabled with an offset of 0.0. Each data point was the sum of 20 spectra, acquired with 50 laser shots each. External calibration was carried out with a set of synthetic peptides (Sequazyme Peptide Mass Standards Kit, Calibration Mixture 3, AB SCIEX).

The metallic and organic composition of samples was determined by thermal and elemental analysis. Thermal analysis of AuZwTriMan was performed by Thermogravimetry (TG) and differential scanning calorimetry (DSC) using a METTLER TOLEDO model TGA/DSC 1 between 30 and 850 °C at 10 °C/min with an air flux at 50 mL/min. Elemental analysis was estimated by inductively coupled plasma high-resolution mass spectrometry (ICP-HRMS) on an ELEMENT XS (Thermo Fisher). Gold and sulfur concentration was determined with Thermo Element software (Thermo Fisher).

Au NC hydrodynamic diameters and ζ-potentials in water, phosphate-buffered saline (PBS), and RPMI 1640 + 10% fetal calf serum (FCS) were analyzed using a Nano ZS Zetasizer (Malvern). Absorption spectra over a 190–900 nm range were collected using a Cary 100 Bio UV–visible spectrophotometer (Varian). Steady-state fluorescence measurements were obtained with diluted samples on a PerkinElmer LS45 fluorescence spectrometer. Fluorescence lifetime measurements were carried out on an Edinburgh Instruments FLS920 fluorometer equipped with an EPL-375 Edinburgh Instrument laser. Spectra were registered with excitation at 374.65 nm and emission detected at 680 nm (slits = 8 nm).

Generation of Monocyte-Derived DCs. Fresh peripheral blood mononuclear cells, obtained by a ficoll gradient, from 40 mL of blood per individual, were used for monocyte purification by means of anti-CD14 microbeads following the manufacturer's protocol (Miltenyi Biotec). The CD14$^-$ cell fraction was placed in 10% dimethyl sulfoxide and frozen for a later lymphocyte proliferation test. To generate DCs, monocytes (CD14$^+$ cells) were incubated in complete medium (CM) containing Roswell Park Memorial Institute 1640 medium (Life Technologies) supplemented with 10% FCS (Life Technologies), streptomycin (100 μg mL^{-1}), and gentamicin (1.25 U mL^{-1}), as well as recombinant human rhGM-CSF (200 ng mL^{-1}) and rhIL-4 (100 ng mL^{-1}) (both from R&D Systems Inc.) for 5 days at 37 °C and 5% CO_2. The resulting DCs were then recovered and used in the experiments.

Gold Concentration in DCs. Quantification of Au NCs in DCs was estimated by ICP-HRMS on an ELEMENT XS (Thermo Fisher) after digesting cells (average of 70 000 cells per sample) with strong acid. The gold concentration in μg/L was determined with Thermo Element software (Thermo Fisher).

Flow-Cytometry-Based Detection of Au-NC-Containing DCs. DCs were incubated at 1×10^5 cells/well in 96-well plates (Nunc, Roskilde, Denmark) with Au NCs at 1, 5, 10, and 25 μg mL^{-1} concentrations in CM for 3 and 48 h at 37 °C. Cells were then analyzed using a FACSCanto II flow cytometer (BD Biosciences) selecting a detection window between 720 and 860 nm, and the data were processed using FLOWJO software (Tree Star, Inc.).

Cell Toxicity Analyses. The cytotoxic effects of Au NCs on DCs were determined by flow cytometry. Typically, 1×10^5 of DCs were incubated with NCs at 1, 5, 10, and 25 μg mL^{-1} in CM for 48 h at 37 °C and 5% CO_2. After incubation, cells were stained with Live/Dead

DOI: 10.1021/acsami.5b06541
ACS Appl. Mater. Interfaces 2015, 7, 20945–20956

NearIR (Life Technologies-Invitrogen) for 15−20 min. Cells were then assessed by flow cytometry (FACSCanto II flow cytometer, BD Biosciences) using a laser excitation wavelength of 633 nm to measure the distribution of fluorescence emissions. Data were analyzed using FLOWJO software (Tree Star, Inc.). The cytotoxicity of NCs on DCs is expressed as a percentage of live cells in experimental samples versus untreated cells.

Ethical Statement. This study was approved by the institutional review board "Comisión de Ética y de Investigación del Hospital Regional Universitario de Málaga", and the experiments were carried out in accordance with the Declaration of Helsinki. Oral and written informed consents for all the procedures were obtained from the subjects included in the study.

Confocal Laser Microscopy (CLSM). Following incubation with Au NCs, DCs were fixed in PBS containing 4% paraformaldehyde for 1 h, washed three times with PBS, and stored protected from light at 4 °C until analysis. Submembrane actin and nuclei (DNA) were labeled by ∼20 min incubations with 10 μM Atto 488-conjugated phalloidin (Sigma) and 1 μg/mL Hoechst 33258 (Sigma), respectively. Once prepared, DCs were either mounted on glass slides in Fluoroshield mounting medium (Sigma) or transferred to optical bottom 96-well plates (Nunc) in PBS for observation by CLSM. For the lysosome staining, after fixation, cells were permeabilized with saponin (0.1% in PBS with 2% bovine serum albumin V fraction (Sigma) followed by an overnight incubation at 4 °C with the primary rabbit LAMP-1 (Santa Cruz Biotechnology) antibody using a 1:25 dilution followed by a 1 h incubation at room temperature with a secondary anti-rabbit Cy2-conjugated antibody (Jackson Laboratories). Cells were washed three times after each antibody incubation and finally mounted on glass slides. Samples were analyzed using a Leica DM6000 inverted microscope connected to a Leica SP5 laser scanning confocal system. For the calculation of Au NC fluorescence intensities, single optical sections were captured from unstained DCs using excitation at 488 nm and detection of Au NC fluorescence emissions between 580 and 700 nm, with an independent bright-field channel (transmitted light) to allow cell detection. For DCs stained with phalloidin, fluorescence from Atto 488 and Au NC was detected simultaneously using 488 nm excitation with a ∼495−520 nm detection window for Atto 488 and ∼600−700 nm for Au NCs (red-shifted to avoid cross-talk from Atto 488). Hoechst 33258 was measured using 405 nm excitation with a 415−470 nm detection window (measured sequentially to avoid cross-talk in other channels).

Transmission Electron Microscopy (TEM). Au NC images were obtained on a FEI Tecnai G2 Twin TEM at 200 kV. TEM samples were prepared by placing a drop of Au NC solution onto a copper grid covered with holey carbon films. Briefly, cells were fixed in a mixture of 2% paraformaldehyde−2.5% glutaraldehyde−0.2 M sucrose in PBS at 4 °C, overnight. After centrifugation, cell pellets were embedded in 10% gelatin, which was solidified at 4 °C and cut into small blocks. After washing with PB, blocks were postfixed in 1% buffered osmium tetroxide for 1 h at room temperature, rinsed in distilled water, and dehydrated in an ethanol series, followed by embedding in low-viscosity Spurr's resin (Electron Microscopy Sciences). Ultrathin sections (70 nm) were obtained with a Leica EM UC-7 ultramicrotome at room temperature. Electron micrographs were obtained in a Tecnai G2 20 Twin (FEI) at 100 kV, with a 4 megapixels Veleta wide-angle camera (Olympus) for general imaging and a 16 megapixel Eagle on-axis camera (FEI) for high-resolution images, using TIA software (FEI).

Cell Experiment with Pharmacological Inhibitors. To study the mechanism involved in Au NC uptake, we selected the following inhibitors and experimentally determined their optimal concentrations: 5 μg mL^{-1} (10 μM) cytochalasin D (CytD), 10 μg mL^{-1} (25 μM) 5-(*N*-ethyl-*N*-isopropyl)hydrochloride (EIPA), 10 μg mL^{-1} (33 μM) nocodazole, 10 μg mL^{-1} (28.1 μM) chlorpromazine hydrochloride, 10 μg mL^{-1} (40 μM) dynasore, and 100 μg mL^{-1} mannan. First, 6×10^5 DCs/well were pretreated with the different inhibitors for 30 min, and then they were incubated with Au NCs at 10 and 25 μg/mL concentrations for 8 h in CM at 37 °C. Cells were analyzed by flow cytometry and confocal microscopy using the same settings as described for the concentration experiment. Toxicity tests in the presence of the inhibitors were performed with the Live/Dead NearIR stain. Data were obtained from two independent sets of experiments each using cells from three different patients.

RESULTS AND DISCUSSION

Au NC Characterization. The NCs AuZw and AuZwTriMan were prepared according to the crystal growth/reduction method using Zw and TriMan molecules as protecting agents (Figure 1).

Both TriMan and Zw can interact with gold species via their mono- or bidentate thiol groups, respectively. Due to the high molar Au:Ligand ratio used during synthesis, dialysis was performed to remove remaining free ligand and prevent self-aggregation of the thiolated ligands. Spectroscopic analyses of AuZwTriMan by NMR and FTIR (Figures S3 and S4, SI) confirmed the presence of the zwitterionic and carbohydrate molecules. Mass spectrometry (MALDI-Tof) experiments were performed on AuZw and AuZwTriMan samples using reflective and linear positive modes to obtain information on the carbohydrate ligand and the Au NCs, respectively. Our measurements in reflective mode detected the monomer signal for the trivalent mannose ligand at m/z = 1190.35 with a small amount of the initial dithiol mannose compound ligand at m/z = 2377.66, indicating the reduction of the dimers during synthesis (Figure S5, SI). The measurements carried out in linear mode confirmed the presence of multiple peaks corresponding to fragmented AuZw and AuZwTriMan NCs in the same mass range, with a maximum mass of m/z ∼7000 (Figure S6, SI). This may indicate a similar size or structure for both NCs, where the low amount of carbohydrate added for the synthesis of AuZwTriMan does not seem to significantly influence NC growth. However, we observed a shift of the broad band centered from ∼14 kDa for AuZw to ∼17 kDa for AuZwTriMan. This band most likely corresponds to ligand-stabilized-Au NCs with the higher molecular weight of TriMan versus Zw explaining the size difference. PAGE electrophoresis revealed that both fluorescent NCs migrate at ∼10 kDa but with a slightly higher size distribution for AuZwTriMan (Figure S7, SI). This observation seems to be in agreement with the mass spectrometry measurements. It should be noted that species >10 kDa were not visible by UV illumination, suggesting that these larger particles emit little or no fluorescence. Chemical analyses of AuZwTriMan and AuZw by thermogravimetry and elemental analysis are shown in Table 1.

Our results show the high organic content of the sample AuZwTriMan (>80 wt %) and an Au:S molar ratio of 1:12.5, which is significantly higher than the 1:1 ratio suggested by the formation of organic multilayers stabilized by covalent (disulfide) and electrostatic interactions on the metal surface similar to previously reported supramolecular assemblies.[36] To

Table 1. Chemical Characterisation of the AuZwTriMan and AuZw NCs

	wt % organic moiety[a]	wt % of Man[b]	Au:S[c]	M[d] (kDa)
AuZw	80 ± 3	0	1:8.9	∼14
AuZwTriMan	83 ± 3	8 ± 2	1:12.5	∼ 17

[a]Determined by thermogravimetry. [b]Determined by the anthrone test. [c]Measurements performed by ICP. [d]Molecular weight estimated for the fluorescent Au NCs by MALDI/Tof analyses.

DOI: 10.1021/acsami.5b06541
ACS Appl. Mater. Interfaces 2015, 7, 20945−20956

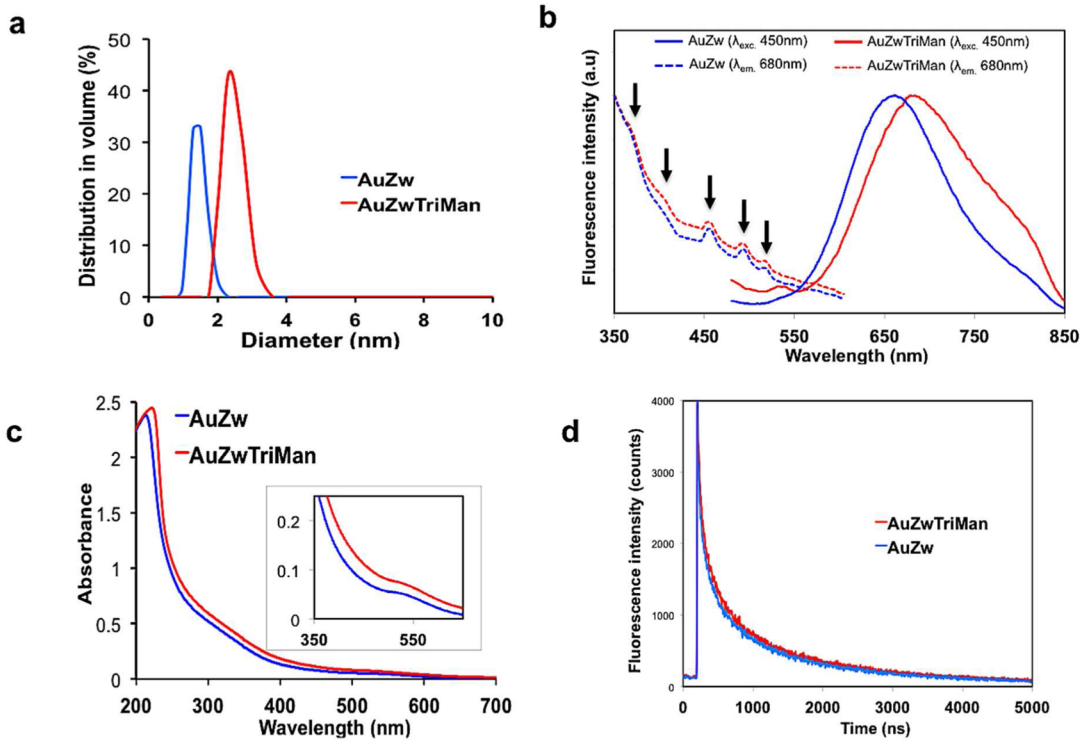

Figure 2. (a) Size measurements of AuZw and AuZwTriMan in water by dynamic light scattering (DLS). (b) Excitation (dashed line, λ_{em} = 680 nm) and emission (solid line, λ_{exc} = 450 nm) spectra of AuZwTriMan and AuZw dispersed in water. Both Au NCs emitted in the red−NIR window with the typical multiple excitation peaks (370, 405, 470, 495 nm, arrows) of Au NCs. (c) The absorbance profiles of diluted AuZw and AuZwTriMan solutions exhibited strong absorbance in the UV region and a shoulder between 400 and 500 nm (inset). (d) Fluorescence lifetime decay of AuZwTriMan and AuZw sols. $\lambda_{exc}/\lambda_{em}$ = 374.8 nm/680 nm.

Table 2. Optical Properties of the AuZwTriMan and AuZw NCs

		relative fluorescence intensity[b]		lifetime		
	λ_{em}[a] (nm)	water	PBS (10 mM, pH 7.2)	water	PBS (10 mM, pH 7.2)	ϕ[c]
AuZw	665	1	0.97	τ_1 = 1.53 μs (85%); τ_2 = 312 ns (15%)	τ_1 = 1.93 μs (73%); τ_2 = 529 ns (27%)	11.3
AuZwTriMan	680	0.89	0.79	τ_1 = 1.50 μs (85%); τ_2 = 300 ns (15%)	τ_1 = 1.90 μs (69%); τ_2 = 541 ns (27%)	8.7

[a]λ_{exc} = 450 nm; [b]Normalized to AuZw fluorescence intensity. Both NCs have an absorbance of 0.1 at λ_{exc} = 450 nm. [c]Determined by comparison with fluorescein (ϕ = 0.79 in 0.1 M NaOH).

quantify the amount of TriMan carbohydrate in AuZwTriMan NCs, we used the colorimetric anthrone test (Figure S8, SI), which determined that trivalent mannose accounts for approximately 8% of the total organic weight. Transmission electronic microscopy (TEM) images of AuZwTriMan and AuZw (Figure S9, SI) showed only particles with diameters <3 nm. Dynamic light scattering (DLS) confirmed the small size of AuZw (ϕ = 1.3 ± 0.5 nm) and AuZwTriMan (ϕ = 2.7 ± 0.5 nm) in water (Figure 2a). The ζ-potentials for AuZw and AuZwTriMan were similar in water and in PBS buffer (10 mM, pH 7.4) with values around −20 mV. The negative charge of the Au NCs could be attributed to the presence of sulfur trioxide from Zw and hydroxyl groups from TriMan. Lowering the pH to 4 resulted in neutral AuZwTriMan species and even slightly positively charged ones in the case of AuZw, but this did not generate detectable precipitation from either NC over a period of 6 months (data not shown). This suggests that both NCs possess strong colloidal stability.

The optical features of AuZwTriMan sol are similar to those of AuZw (Figures 2b), with a broad fluorescence emission in the red−NIR region ($\lambda_{em.}$ = 680 nm) and the presence of multiple excitation bands (370, 400, 450, 490, and 515 nm) associated with intra and inter energy electronic transitions. Such broad emissions are quite common for Au NCs and are related to the presence of multiple atomic species. We found that high TriMan concentrations resulted in decreased fluorescence intensities (Figure S10, SI). Therefore, we determined an optimal Au:Zw:$NaBH_4$:TriMan ratio of 1:10:2:0.21, which resulted in a relatively high level of fluorescence with an intensity loss of less than 20% with respect to AuZw and colloidal stability in vitro. The effect of high TriMan concentrations could be attributed to strong interactions between Au^{III} and TriMan OH groups and TriMan's large size relative to Zw causing steric hindrance that prevents the growth of fluorescent Au NCs. The relative amounts of two different ligands have recently been shown to influence the size and shell structure of Ag-doped Au NCs, dramatically affecting their optical properties.[54] The red-shift of AuZwTriMan fluorescence could be attributed either to an altered average core size, according to the jellium model,[32] or to changes to the metal surface following addition of the carbohydrate ligand. Indeed, with respect to the latter possibility, several studies have shown that ligand nature can affect red−NIR region photoluminescence.[38,55] The excitation

DOI: 10.1021/acsami.5b06541
ACS Appl. Mater. Interfaces 2015, 7, 20945−20956

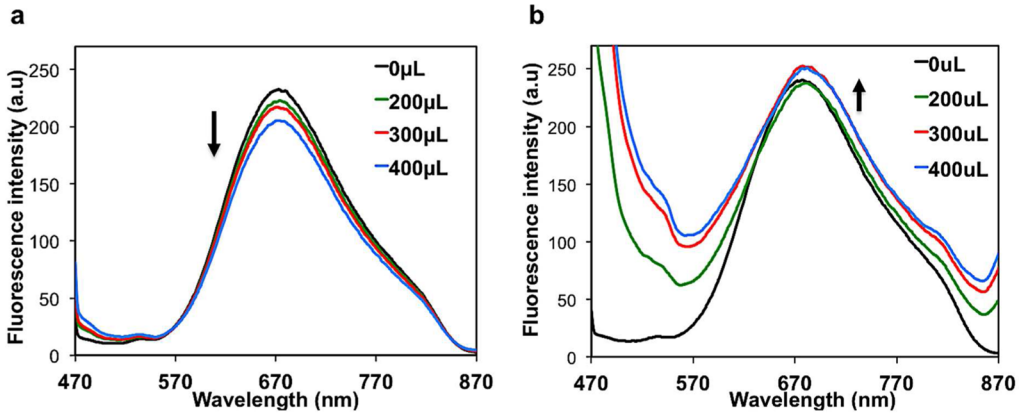

c

	AuZw			AuZwTriMan		
ConA (5mg.mL^{-1})	0µL	50µL	100µL	0µL	50µL	100µL
τ1	529ns (27%)	512ns (26%)	518ns (25%)	565ns (31%)	541ns (27%)	378ns (18%)
τ2	1.93µs (73%)	1.92µs (74%)	1.88µs (75%)	1.90µs (69%)	1.78µs (73%)	1.51µs (82%)
χ	1.067	1.091	0.936	1.120	1.200	1.141

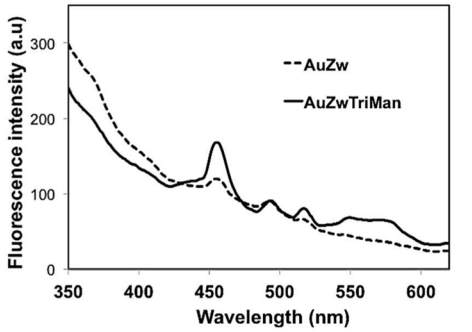

Figure 3. Fluorescence emission of AuZw (a) and AuZwTriMan (b) dispersed in PBS buffer (10 mM, pH 7.4) with ([Ca^{2+}] = [Mn^{2+}] = 0.1 mM) after the addition of ConA (5 mg mL^{-1}). λ_{exc} = 450 nm. (c) Fluorescence lifetime data of AuZw and AuZwTriMan in the presence of ConA (5 mg mL^{-1}) under the same conditions as previously described. λ_{exc} = 374.65 nm, λ_{em} = 680 nm. (d) Excitation spectra of AuZw (dashed line) and AuZwTriMan (solid line) after the addition of ConA (5 mg mL^{-1}). λ_{em} = 680 nm.

peaks for the two Au NCs are located similarly to those reported for other Au NCs stabilized by thiol linkers, regardless of the terminal groups used.[55] The absorbance spectra of AuZwTriMan and AuZw sols show strong UV absorption, with the presence of broad and weak bands between 400 and 500 nm (Figure 2c). Fluorescence lifetime measurements of AuZwTriMan in water show a biexponential behavior of τ_1 = 300 ns (15%) and τ_2 = 1.5 μs (85%) with a microsecond range lifetime characteristic of the metal−ligand electronic transition (Figure 2d).[44,56] The short nanosecond range lifetime is usually associated with singlet excited states originating from metal−metal interactions. On the other hand, the long microsecond range lifetime component is typical of triplet excited states.[43,57] This extended high-energy state is of interest for analytical applications due to its high sensitivity to the local environment. The most important optical features of AuZw and AuZwTriMan are summarized in Table 2.

In order to verify the activity of the trivalent mannose present on the surface of the AuZwTriMan metal core, a simple test was performed by adding the lectin concanavalin A (ConA, 5 mg mL^{-1}) to diluted sols of AuZw and AuZwTriMan in PBS buffer (10 mM, pH 7.4) in the presence of calcium and magnesium ions ([Ca^{2+}] = [Mn^{2+}] = 0.1 mM). Only AuZwTriMan became more turbid in the presence of ConA, indicating aggregate formation (data not shown). AuZw fluorescence decreased evenly upon adding ConA (Figure 3a). In contrast, the addition of ConA increased AuZwTriMan fluorescence at λ = 685 nm, accompanied by a small red-shift (Figure 3b). Aggregation-induced increases in fluorescence intensity at shorter wavelengths have recently been reported.[45] The phenomenon of aggregation-induced emission (AIE) is well-documented for organic luminophores[58] but has only recently been reported for metal (Au, Cu) nanoclusters.[45,59] For instance, in an elegant study from the Xie laboratory, it was shown that Au NC aggregation induced by the presence of ethanol or by electrostatic interactions in the presence of cadmium cations led to a drastic fluorescent enhancement.[45] It was proposed that the strong fluorescence of the dense aggregates was generated by both inter/intra complex aurophilic interactions and by the reduced intramolecular motion of the complex. In our case, the AIE of AuZwTriMan emissions are likely to be the result of electrostatic interactions between the lectin and the carbohydrate ligand, as the NC core is strongly protected by a saturation of mono- and bidentate thiol ligands.

We expected that the long fluorescence lifetime of Au NCs would be sensitive to their aggregation state. Indeed, their fluorescence lifetime was longer in PBS buffer than in deionized water (Table 2), probably due to Au NC cross-linking induced by the presence of salts. Moreover, we found that the microsecond range (τ_2) fluorescence lifetime of AuZwTriMan was strongly influenced by the presence of ConA, dropping from 1.91 to 1.51 μs, while no change was observed for AuZw (Figure 3c). This decrease could be attributed to the combined contribution of NC local polarity changes and enhanced network rigidity induced by the formation of dense aggregates. The NC cross-linking hypothesis is consistent with the altered excitation spectrum profile of AuZwTriMan in the presence of ConA (Figure 3d). In fact, the AuZwTriMan λ = 450 nm excitation peak increased significantly relative the AuZw equivalent, in addition to the appearance of two new peaks at longer wavelength (λ = 545 and 575 nm). The 450 nm band

DOI: 10.1021/acsami.5b06541
ACS Appl. Mater. Interfaces 2015, 7, 20945−20956

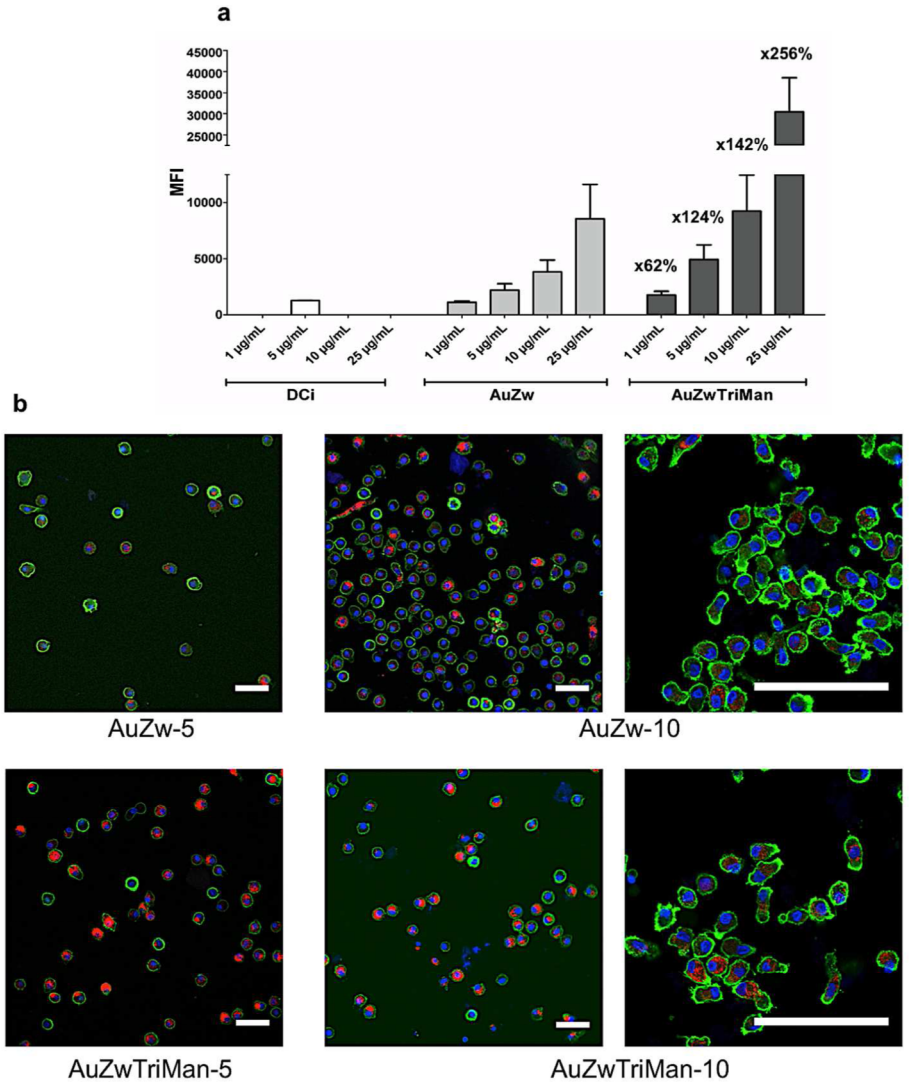

Figure 4. (a) Flow cytometry measurements of DCs incubated with AuZw and AuZwTriMan at different concentrations (1, 5, 10, and 25 μg mL^{-1} in CM) for 48 h (MFI: mean fluorescence intensity). Results showed the strong enhancement of particle uptake for Au NCs containing the mannose ligand. (b) CLSM images of DCs incubated with AuZw and AuZwTriMan at 5 and 10 μg mL^{-1} in CM for 48 h. Bars: 100 μm. Data are consistent with the flow cytometry analysis showing a higher fluorescence signal (red) from AuZwTriMan than for AuZw inside the cells at the same concentration. Submembrane actin was stained postfixation with Atto 488−phalloidin (green) and nuclei with Hoechst (blue).

has been mainly associated with different gold magic cluster to electronic interband transitions (sp ← d) that are strongly involved in ligand-to-metal charge transfers (LMCTs) or ligand to metal−metal charge transfers (LMMCTs).[55] Therefore, the aggregation triggered by ConA could be responsible for a rearrangement of the polymeric monolayer that protects the NC gold core. However, the complexity of the photoluminescence mechanisms occurring in this system via multiple intra- and interelectronic transitions will require further investigation, especially by looking at the properties of monodisperse single metal NCs. In summary, the enhanced fluorescence emissions and decreased fluorescence lifetime of AuZwTriMan are consistent with its aggregation in the presence of ConA, confirming specific binding between lectin and the carbohydrate ligand.

The colloidal stability of AuZwTriMan and AuZw dispersed in CM (RPMI 1640 + 10% FCS) was determined by DLS over 48 h. Particles rapidly increased to ∼10 nm, probably due to protein corona formation, but did not show any significant aggregation (Figure S11, SI). The presence of protein in the CM influenced Au NC surface charge, with their ζ-potential shifting from −20 to −10 mV. Fluorescence measurements carried out in CM confirmed the relatively high optical stability of both NCs (Figure S12, SI) over 48 h.

Au NC Cellular Accumulation. In order to determine the influence of the trivalent mannose linker on Au NC−DC interactions, different concentrations of AuZwTriMan and AuZw from 1 to 25 μg mL^{-1} were incubated with DCs for 3 or 48 h and studied by several techniques. Au NCs could be quantified and localized by flow cytometry and confocal laser scanning microscopy (CLSM) even at low concentrations thanks to their fluorescence emission in the NIR region and high Stokes shift.[41,44] Flow cytometry measurements shown in Figure 4a indicate that AuZwTriMan and AuZw were uptaken by DCs in a dose-dependent manner after 48 h. However, the uptake of AuZwTriMan NCs was 62% (1.62-fold) stronger than for AuZw at 1 μg mL^{-1} gold concentration and by 256% (3.56-fold) at 25 μg mL^{-1}. These results strongly suggest that the presence of TriMan promotes NC-enhanced uptake in DCs. However, as fluorescence might be affected by the local

DOI: 10.1021/acsami.5b06541
ACS Appl. Mater. Interfaces 2015, 7, 20945−20956

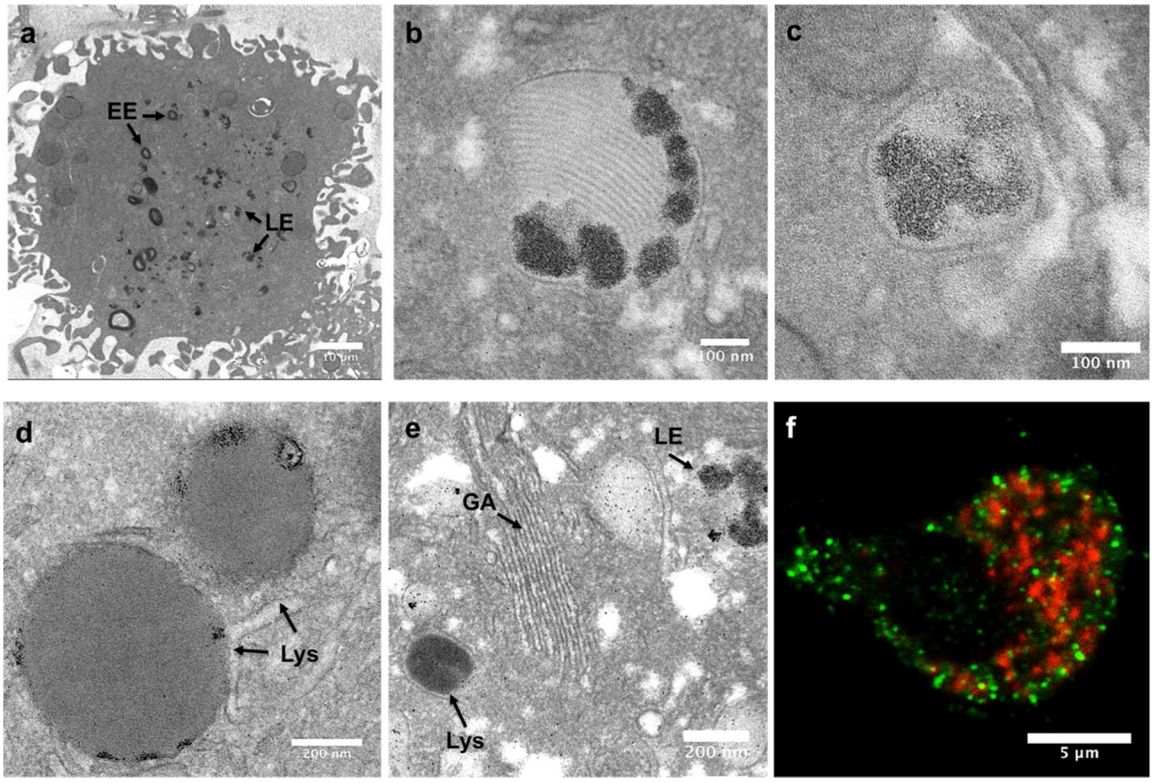

Figure 5. Electron microscopy images of DCs incubated with AuZwTriMan (25 μg mL^{-1} in CM for 48 h) showing the presence of Au NCs (dark dots) in several types of multilaminar and amorphous organelles (a–c) from early endosomes (EE) (a) and late endosomes (LE) (a, e) to lysosomes (Lys) (d, e) close to the Golgi apparatus (GA) (e). (f) CLSM image of DCs incubated with AuZwTriMan (red) and stained with anti-LAMP-1 (lysosome marker, green) indicating that few LAMP1-positive lysosomes contain detectable levels of AuZwTriMan.

cellular environment (pH, particle aggregation, etc.), we also measured the gold concentration in DCs following incubation with AuZw and AuZwTriMan by inductively coupled plasma (ICP) analysis. This analysis confirmed a higher gold concentration (>75%) in cells incubated with the glyco-Au NC (Figure S13, SI). These results clearly demonstrate a strong enhancement of dendritic cell NC uptake by the presence of the trivalent mannose ligand. Additional experiments found that DC uptake of both AuZwTriMan and AuZw Au NCs continues to increase after 3 h, with higher levels of fluorescence detected after 48 h under most conditions (Figure S14, SI). Interestingly, in the case of AuZwTriMan, more than 50% of cells exhibited detectable fluorescence after 3 h (versus only 12% for AuZw) even at the lower Au NC concentration. The CLSM images, shown in Figure 4b, indicate that NCs were distributed homogeneously in the cells and confirm the flow cytometry data, with a higher uptake of AuZwTriMan than AuZw in DCs at 5 and 10 μg mL^{-1} concentrations after 48 h.

The intracellular distribution of red–NIR-emitting Au NCs in DCs as determined by CLSM (Figure S15, SI) appeared similarly independent of the nature of the ligand, with both particles showing intracellular accumulation in the cytoplasm and strong perinuclear accumulation, as previously reported by our lab.[52] Because both NCs contain a high content of zwitterionic ligand on their surface, the interaction between the particles and DCs will involve mainly electrostatic interactions.[53] TEM micrographs of DCs incubated with AuZwTriMan (25 μg mL^{-1} for 48 h) show an accumulation of Au NCs (dark dots about ~2 nm in size) in different organelles (Figures 5a–c and S16, SI). On the basis of comparisons with previous particle localization studies in DCs,[60,61] we identified AuZwTriMan NCs in early endosomes (a), late endosomes (a, e), and lysosomes (d, e) close to the Golgi apparatus (e), which is consistent with their uptake via endocytic pathways. Experiments with the lysosome marker LAMP-1 indicate that a relatively low proportion of Au NCs colocalize with lysosomes (Figure 5f). However, it is important to point out that only fluorescence from relatively large NC aggregates is likely to be detectable by confocal microscopy.

Cell Toxicity. Next we incubated AuZw and AuZwTriMan with DCs at different concentrations (1–25 μg mL^{-1}) and different incubation times (3 and 48 h). Cytometry-based live/dead cell viability assays did not detect any significant toxicity above the threshold by flow cytometry measurement in any of the tested conditions (data not shown). This is consistent with the absence of Au NC cytotoxicity described in previous studies using several in vitro and in vivo models.[49,50]

Au NC Uptake Mechanisms. Endocytosis refers to a conserved process whereby macromolecules or solutes are taken up by cells via the invagination of plasma membrane to form vesicles.[62] NPs with size <200 nm are usually uptaken via endocytic pathways that can be divided into different classes: clathrin-dependent, caveolae, macropinocytosis, and clathrin- and caveolae-independent endocytosis.[63] After endocytosis, NPs tend to be contained within different types of intracellular vesicles, some of which can subsequently fuse with lysosomes, where they accumulate until they are eventually degraded.[63] It has been established that cellular NP uptake mechanisms are dependent on the physicochemical parameters (size, shape, charge, hydrophobicity) of NPs, and on the cell type studied. To gain more insight into the mechanisms involved in DC uptake of Au NCs stabilized by the Zw and TriMan ligands, we

DOI: 10.1021/acsami.5b06541
ACS Appl. Mater. Interfaces 2015, 7, 20945–20956

selected a series of different inhibitors that differentially affect the endocytic pathways mentioned above. To optimize inhibitor concentration, we first tested different levels of each inhibitor with DCs, with and without Au NPs, and selected the highest concentration that did not induce detectable cytotoxicity (Figure S17, SI; data not shown). CLSM was also used to ensure an intact cell cytoskeleton (except for actin and tubulin depolymerization using CytD and nocodazole, respectively) at different concentrations (Figure S18, SI; data not shown). We selected an 8 h Au NC incubation time as a compromise between a short incubation time to avoid multiple uptake mechanisms and having enough fluorescent signal for cell analysis.

The inhibitor experiments showed consistent results using 10 and 25 μg mL^{-1} of Au NCs, indicating no saturation of cell uptake in this particle concentration range (Figure S19, SI). Mannan is a compound commonly chosen as an inhibitor to confirm specific cell uptake by C-lectin receptors such as MR and DC-SIGN. Flow cytometry measurements showed a 60% reduction in Au NC uptake for AuZwTriMan (Figure 6), while

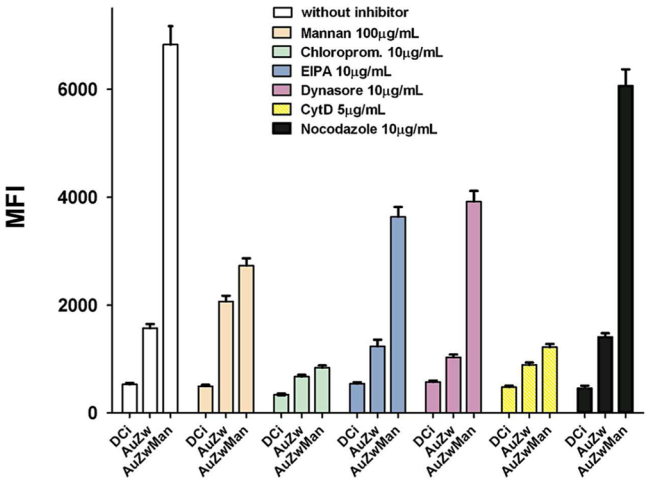

Figure 6. Endocytic pathway inhibitor experiments. DCs were pretreated with the inhibitors for 30 min and then incubated for 8 h with either AuZw or AuZwTriMan (25 μg mL^{-1} in CM). Fluorescence was measured by flow cytometry and expressed as mean fluorescence intensity (MFI).

mannan had no effect on AuZw uptake. These data clearly demonstrate the highly specific uptake of AuZwTriMan by C-lectin receptors. This is consistent with the well-known interaction between mannose molecules and the different types of C-lectin receptors (MR, DC-SIGN) present on the DC surface.[61] The remarkable C-lectin-dependent uptake of AuZwTriMan by DCs might also be attributed to the strong affinity of DC lectin receptors for the multivalent TriMan ligand.

A second inhibitor, chlorpromazine hydrochloride, was used to determine if Au NCs are processed by clathrin-mediated endocytosis (CME). Chlorpromazine is a cationic amphiphilic class drug and an inhibitor of the clathrin-coated pit pathway. Chlorpromazine is known to cause a loss of coated pits and associated receptors from the cell surface, resulting in the accumulation of clathrin and AP-2 in endosomal compartments.[64] Results showed 88% and 57% decreases for AuZwTriMan and AuZw, respectively, indicating that CME is an important pathway for their uptake by DCs. To confirm this, we tested a dynamin inhibitor, dynasore, as dynamin is essential for clathrin-coated vesicle formation.[65] Dynasore tends to interfere with the GTPase activity of dynamin and suppresses the pinching-off process but not the formation of clathrin-coated pits, in contrast to chlorpromazine.[66] Dynasore decreased the uptake of AuZwTriMan and AuZw by 42% and 59%, respectively, confirming the importance of clathrin in initiating endocytosis for both Au NCs.

EIPA, an inhibitor of macropinocytosis, reduced AuZwTriMan uptake by 47% and AuZw uptake by 21%. Macropinocytosis is a form of endocytosis that involves coordinated cytoskeletal changes at the cell surface.[67] This result seems to suggest a less significant contribution for macropinocytosis in NC processing than that reported in other studies, which have ascribed macropinocytosis a major role in the engulfment of NPs by macrophages such as DCs.[63] CytD is a drug that can depolymerise F-actin filaments and disrupt the cytoskeleton. CytD has been reported to interfere with macropinocytosis and caveolae-dependent uptake without affecting CME.[63] Treatment with CytD induced a strong 82% decrease in AuZwTriMan uptake and a 43% decrease for AuZw. However, results from CytD treatment need to be interpreted with caution, as its action is extremely broad, affecting all endocytic pathways and as well as many other biological processes.[68] Our results suggest that the actin cytoskeleton plays a key role in Au NC endocytosis, which is in agreement with the results of uptake mechanism studies performed on different types of NP (quantum dots,[69] polystyrene,[70] chitosan[62]) with sizes smaller than 50 nm in DCs. Our results suggest that the endocytic uptake of AuZw by DCs occurs via multiple mechanisms with major roles for clathrin- and F-actin-dependent endocytic pathways. Similar DC uptake behavior has been reported by Zhang and colleagues using carboxyl-coated quantum dots (ϕ = 18 nm).[69]

Microtubules are a major class of cytoskeletal fiber, responsible for vesicular trafficking among many other biological functions. The nocodazole inhibitor, which disrupts the microtubule cytoskeleton, did not strongly affect the DC uptake of either type of Au NC, with an 11% decrease in both cases. This is consistent with a study performed by Dawson and co-workers that showed that microtubule function was required for the uptake of larger (200 nm) but not smaller (40 nm) NPs.[70]

CONCLUSIONS

In summary, Au NCs stabilized by a mixture of zwitterionic and trivalent mannose ligands were prepared using the crystal growth/reduction method. Chemical and optical characterization confirmed their ultrasmall size ($\phi \sim 2$ nm), fluorescence emission in the red−NIR window, and the activity of their carbohydrate ligands. Interestingly, an aggregation-induced emission enhancement was observed for Au NCs coated with the mannose ligand in the presence of the lectin ConA. Measurements of Au NCs dispersed in complete medium showed relatively high colloidal and fluorescence stability. Studies in DCs showed a greater than 2.5-fold increase in particle uptake when stabilized by a trivalent mannose ligand versus a zwitterionic ligand alone. Experiments using inhibitors that target different uptake mechanisms suggest that DCs uptake Au NCs via multiple endocytic pathways, with major roles for clathrin-mediated and F-actin-dependent mechanisms. The 60% reduction in the uptake of mannose-coated Au NCs by the presence of a C-lectin inhibitor clearly demonstrates the

DOI: 10.1021/acsami.5b06541
ACS Appl. Mater. Interfaces 2015, 7, 20945−20956

specific targeting of Au NCs to DCs via C-lectin receptors. Electron microscopy data support the hypothesis that Au NCs are engulfed by endocytosis, with particles present in both endosomes and lysosomes.

Regarding future applications, carbohydrate-ligand-stabilized gold nanoclusters have great potential as a delivery system due to their low cytotoxicity, good colloidal stability, and strong uptake in DCs at very low concentrations (1 $\mu g\ mL^{-1}$) thanks to their interaction with C-lectin receptors on the DC surface and their ultrasmall size (i.e., high diffusion). The original optical properties of NCs allow them to be visualized by fluorescence in the red−NIR window and potentially by other techniques, such as X-ray tomography or photoacoustic imaging, as well as exploited for their photothermal properties due to their gold nature.

■ ASSOCIATED CONTENT

Supporting Information

The Supporting Information is available free of charge on the ACS Publications website at DOI: 10.1021/acsami.5b06541.

Ligand synthesis and characterization; additional chemical and optical characterization of NCs; cell studies, including cytotoxicity and inhibitory experiments; and Figures S1−S19 (PDF)

■ AUTHOR INFORMATION

Corresponding Author

*E-mail: xleguevel@bionand.es. Tel: +34 952 367 648. Fax: +34 952 367 610.

Notes

The authors declare no competing financial interest.

■ ACKNOWLEDGMENTS

This work was supported by the Instituto de Salud Carlos III (ISCII) (project no. CP12/03310) and by the Ministerio de Economía y Competitividad (MINECO) (CTQ2011-23410 and CTQ2014-52328-P) and cofinanced by European Regional Development Fund (ERDF) and by ISCIII-Thematic Networks and Co-operative Research Centers: RIRAAF (RD012/0013), Junta de Andalucía (CTS-7433), ISCIII (PI12/02481-PI/02529), and the Nicolas Monardes Program (C-0044-2012 SAS2013). X.L.G. would like to thank Daniel Sierra for the zwitterion ligand synthesis, Carlos Rodriguez for the mass spectrometry analysis, José Maria Montenegro for the fluorescence lifetime measurement, Juan Felix Lopez (BIONAND Nanoimaging Unit) for the TEM measurements, and John Pearson (BIONAND Nanoimaging Unit) for the optical microscopy analysis and critical reading of the manuscript.

■ REFERENCES

(1) Cruz, L. J.; Tacken, P. J.; Fokkink, R.; Joosten, B.; Stuart, M. C.; Albericio, F.; Torensma, R.; Figdor, C. G. Targeted PLGA Nano- but not Microparticles specifically deliver Antigen to human Dendritic Cells via DC-SIGN In Vitro. *J. Controlled Release* **2010**, *144* (2), 118−126.

(2) Marradi, M.; Chiodo, F.; García, I.; Penadés, S. Glyconanoparticles as Multifunctional and Multimodal Carbohydrate Systems. *Chem. Soc. Rev.* **2013**, *42* (11), 4728−4745.

(3) Novak, N. Targeting Dendritic Cells in Allergen Immunotherapy. *Immunol. Allergy Clin. North Am.* **2006**, *26* (2), 307−319.

(4) Abbas, A. K.; Sharpe, A. H. Dendritic Cells giveth and taketh away. *Nat. Immunol.* **2005**, *6* (3), 227−228.

(5) Mellman, I.; Steinman, R. M. Dendritic cells: Specialized and Regulated Antigen Processing Machines. *Cell* **2001**, *106* (3), 255−258.

(6) Hubbell, J. A.; Thomas, S. N.; Swartz, M. A. Materials Engineering for Immunomodulation. *Nature* **2009**, *462* (7272), 449−460.

(7) Kim, J.; Mooney, D. J. In Vivo Modulation of Dendritic Cells by Engineered Materials: Towards new Cancer Vaccines. *Nano Today* **2011**, *6* (5), 466−477.

(8) Kreutz, M.; Tacken, P. J.; Figdor, C. G. Targeting Dendritic Cells–why bother? *Blood* **2013**, *121* (15), 2836−2844.

(9) Dobrovolskaia, M. A.; McNeil, S. E. Immunological Properties of Engineered Nanomaterials. *Nat. Nanotechnol.* **2007**, *2* (8), 469−478.

(10) Klippstein, R.; Pozo, D. Nanotechnology-based Manipulation of Dendritic Cells for Enhanced Immunotherapy Strategies. *Nanomedicine* **2010**, *6* (4), 523−529.

(11) Reddy, S. T.; Rehor, A.; Schmoekel, H. G.; Hubbell, J. A.; Swartz, M. A. In Vivo Targeting of Dendritic Cells in Lymph Nodes with poly(propylene sulfide) Nanoparticles. *J. Controlled Release* **2006**, *112* (1), 26−34.

(12) Hirosue, S.; Kourtis, I. C.; van der Vlies, A. J.; Hubbell, J. A.; Swartz, M. A. Antigen Delivery to Dendritic Cells by poly(propylene sulfide) Nanoparticles with disulfide Conjugated Peptides: Cross-Presentation and T cell Activation. *Vaccine* **2010**, *28* (50), 7897−7906.

(13) García-Vallejo, J. J.; Ambrosini, M.; Overbeek, A.; van Riel, W. E.; Bloem, K.; Unger, W. W. J.; Chiodo, F.; Bolscher, J. G.; Nazmi, K.; Kalay, H.; van Kooyk, Y. Multivalent Glycopeptide Dendrimers for the Targeted Delivery of Antigens to Dendritic Cells. *Mol. Immunol.* **2013**, *53* (4), 387−397.

(14) Moffat, J. M.; Cheong, W. S.; Villadangos, J. A.; Mintern, J. D.; Netter, H. J. Hepatitis B Virus-like Particles access major Histocompatibility Class I and II Antigen Presentation Pathways in Primary Dendritic Cells. *Vaccine* **2013**, *31* (18), 2310−2316.

(15) Unger, W. W. J.; Van Beelen, A. J.; Bruijns, S. C.; Joshi, M.; Fehres, C. M.; Van Bloois, L.; Verstege, M. I.; Ambrosini, M.; Kalay, H.; Nazmi, K.; Bolscher, J. G.; Hooijberg, E.; De Gruijl, T. D.; Storm, G.; Van Kooyk, Y. Glycan-modified Liposomes boost CD4 + and CD8 + T-cell Responses by Targeting DC-SIGN on Dendritic Cells. *J. Controlled Release* **2012**, *160* (1), 88−95.

(16) Chiodo, F.; Marradi, M.; Park, J.; Ram, A. F. J.; Penadés, S.; Van Die, I.; Tefsen, B. Galactofuranose-coated Gold Nanoparticles elicit a Pro-inflammatory Response in Human Monocyte-derived Dendritic Cells and are recognized by DC-SIGN. *ACS Chem. Biol.* **2014**, *9* (2), 383−389.

(17) Shahbazi, M. A.; Fernández, T. D.; Mäkilä, E. M.; Le Guével, X.; Mayorga, C.; Kaasalainen, M. H.; Salonen, J. J.; Hirvonen, J. T.; Santos, H. A. Surface Chemistry Dependent Immunostimulative Potential of Porous Silicon Nanoplatforms. *Biomaterials* **2014**, *35* (33), 9224−9235.

(18) Tomić, S.; Dokić, J.; Vasilijić, S.; Ogrinc, N.; Rudolf, R.; Pelicon, P.; Vučević, D.; Milosavljević, P.; Janković, S.; Anžel, I.; Rajković, J.; Rupnik, M. S.; Friedrich, B.; Čolić, M. Size-Dependent Effects of Gold Nanoparticles Uptake on Maturation and Antitumor Functions of Human Dendritic Cells In Vitro. *PLoS One* **2014**, *9* (5), e96584.

(19) Reddy, S. T.; Van Der Vlies, A. J.; Simeoni, E.; Angeli, V.; Randolph, G. J.; O'Neil, C. P.; Lee, L. K.; Swartz, M. A.; Hubbell, J. A. Exploiting Lymphatic Transport and Complement Activation in Nanoparticle Vaccines. *Nat. Biotechnol.* **2007**, *25* (10), 1159−1164.

(20) Huo, S.; Ma, H.; Huang, K.; Liu, J.; Wei, T.; Jin, S.; Zhang, J.; He, S.; Liang, X. J. Superior Penetration and Retention Behavior of 50 nm Gold Nanoparticles in Tumors. *Cancer Res.* **2013**, *73* (1), 319−330.

(21) Hirsjärvi, S.; Dufort, S.; Gravier, J.; Texier, I.; Yan, Q.; Bibette, J.; Sancey, L.; Josserand, V.; Passirani, C.; Benoit, J. P.; Coll, J. L. Influence of Size, Surface Coating and Fine Chemical Composition on the In Vitro Reactivity and In Vivo Biodistribution of Lipid Nanocapsules versus Lipid Nanoemulsions in Cancer Models. *Nanomedicine* **2013**, *9* (3), 375−387.

(22) Moros, M.; Hernáez, B.; Garet, E.; Dias, J. T.; Sáez, B.; Grazú, V.; González-Fernández, A.; Alonso, C.; De La Fuente, J. M.

DOI: 10.1021/acsami.5b06541
ACS Appl. Mater. Interfaces 2015, 7, 20945−20956

Monosaccharides versus PEG-Functionalized NPs: Influence in the Cellular Uptake. *ACS Nano* **2012**, *6* (2), 1565−1577.
(23) Figdor, C. G.; Van Kooyk, Y.; Adema, G. J. C-type Lectin Receptors on Dendritic Cells and Langerhans Cells. *Nat. Rev. Immunol.* **2002**, *2* (2), 77−84.
(24) Bernardi, A.; Jiménez-Barbero, J.; Casnati, A.; De Castro, C.; Darbre, T.; Fieschi, F.; Finne, J.; Funken, H.; Jaeger, K. E.; Lahmann, M.; Lindhorst, T. K.; Marradi, M.; Messner, P.; Molinaro, A.; Murphy, P. V.; Nativi, C.; Oscarson, S.; Penadés, S.; Peri, F.; Pieters, R. J.; Renaudet, O.; Reymond, J. L.; Richichi, B.; Rojo, J.; Sansone, F.; Schäffer, C.; Turnbull, W. B.; Velasco-Torrijos, T.; Vidal, S.; Vincent, S.; Wennekes, T.; Zuilhof, H.; Imberty, A. Multivalent Glycoconjugates as Anti-pathogenic Agents. *Chem. Soc. Rev.* **2013**, *42* (11), 4709−4727.
(25) Ribeiro-Viana, R.; García-Vallejo, J. J.; Collado, D.; Pérez-Inestrosa, E.; Bloem, K.; Van Kooyk, Y.; Rojo, J. BODIPY-labeled DC-SIGN-Targeting Glycodendrons efficiently Internalize and Route to Lysosomes in Human Dendritic Cells. *Biomacromolecules* **2012**, *13* (10), 3209−3219.
(26) Luczkowiak, J.; Muñoz, A.; Sánchez-Navarro, M.; Ribeiro-Viana, R.; Ginieis, A.; Illescas, B. M.; Martín, N.; Delgado, R.; Rojo, J. Glycofullerenes Inhibit Viral Infection. *Biomacromolecules* **2013**, *14* (2), 431−437.
(27) Sattin, S.; Daghetti, A.; Thépaut, M.; Berzi, A.; Sánchez-Navarro, M.; Tabarani, G.; Rojo, J.; Fieschi, F.; Clerici, M.; Bernardi, A. Inhibition of DC-SIGN-Mediated HIV Infection by a Linear Trimannoside mimic in a Tetravalent Presentation. *ACS Chem. Biol.* **2010**, *5* (3), 301−312.
(28) Luczkowiak, J.; Sattin, S.; Sutkevičiute, I.; Reina, J. J.; Sánchez-Navarro, M.; Thépaut, M.; Martínez-Prats, L.; Daghetti, A.; Fieschi, F.; Delgado, R.; Bernardi, A.; Rojo, J. Pseudosaccharide Functionalized Dendrimers as Potent Inhibitors of DC-SIGN Dependent Ebola Pseudotyped Viral Infection. *Bioconjugate Chem.* **2011**, *22* (7), 1354−1365.
(29) Ribeiro-Viana, R.; Sánchez-Navarro, M.; Luczkowiak, J.; Koeppe, J. R.; Delgado, R.; Rojo, J.; Davis, B. G. Virus-like Glycodendrinanoparticles Displaying Quasi-equivalent nested Polyvalency upon Glycoprotein Platforms Potently Block Viral Infection. *Nat. Commun.* **2012**, *3*, 1303.
(30) Jin, R. Quantum sized, Thiolate-protected Gold Nanoclusters. *Nanoscale* **2010**, *2* (3), 343−362.
(31) Zheng, J.; Zhou, C.; Yu, M.; Liu, J. Different Sized Luminescent Gold Nanoparticles. *Nanoscale* **2012**, *4* (14), 4073−4083.
(32) Zheng, J.; Nicovich, P. R.; Dickson, R. M. Highly Fluorescent Noble-Metal Quantum Dots. *Annu. Rev. Phys. Chem.* **2007**, *58*, 409−431.
(33) Goswami, N.; Zheng, K.; Xie, J. Bio-NCs-the Marriage of Ultrasmall Metal Nanoclusters with Biomolecules. *Nanoscale* **2014**, *6* (22), 13328−13347.
(34) Jiang, D. E. The Expanding Universe of Thiolated Gold Nanoclusters and Beyond. *Nanoscale* **2013**, *5* (16), 7149−7160.
(35) Zhu, M.; Aikens, C. M.; Hollander, F. J.; Schatz, G. C.; Jin, R. Correlating the Crystal Structure of a Thiol-protected Au25 Cluster and Optical Properties. *J. Am. Chem. Soc.* **2008**, *130* (18), 5883−5885.
(36) Le Guével, X.; Tagit, O.; Rodríguez, C. E.; Trouillet, V.; Pernia Leal, M.; Hildebrandt, N. Ligand Effect on the Size, Valence State and Red/near Infrared Photoluminescence of Bidentate Thiol Gold Nanoclusters. *Nanoscale* **2014**, *6* (14), 8091−8099.
(37) Negishi, Y.; Nobusada, K.; Tsukuda, T. Glutathione-protected Gold Clusters Revisited: Bridging the Gap between Gold(I)-thiolate Complexes and Thiolate-protected Gold Nanocrystals. *J. Am. Chem. Soc.* **2005**, *127* (14), 5261−5270.
(38) Wang, G.; Guo, R.; Kalyuzhny, G.; Choi, J. P.; Murray, R. W. NIR Luminescence Intensities increase Linearly with Proportion of Polar Thiolate Ligands in Protecting Monolayers of Au 38 and Au 140 Quantum Dots. *J. Phys. Chem. B* **2006**, *110* (41), 20282−20289.
(39) Yu, Y.; Luo, Z.; Chevrier, D. M.; Leong, D. T.; Zhang, P.; Jiang, D. E.; Xie, J. Identification of a Highly Luminescent Au22(SG)18 Nanocluster. *J. Am. Chem. Soc.* **2014**, *136* (4), 1246−1249.
(40) Aldeek, F.; Muhammed, M. A. H.; Palui, G.; Zhan, N.; Mattoussi, H. Growth of Highly Fluorescent Polyethylene glycol- and Zwitterion- Functionalized Gold Nanoclusters. *ACS Nano* **2013**, *7* (3), 2509−2521.
(41) Le Guével, X.; Spies, C.; Daum, N.; Jung, G.; Schneider, M. Highly Fluorescent Silver Nanoclusters Stabilized by Glutathione: A Promising Fluorescent Label for Bioimaging. *Nano Res.* **2012**, *5* (6), 379−387.
(42) Muhammed, M. A. H.; Ramesh, S.; Sinha, S. S.; Pal, S. K.; Pradeep, T. Two Distinct Fluorescent Quantum Clusters of Gold Starting from Metallic Nanoparticles by pH-Dependent Ligand Etching. *Nano Res.* **2008**, *1*, 333−340.
(43) Le Guével, X.; Hötzer, B.; Jung, G.; Hollemeyer, K.; Trouillet, V.; Schneider, M. Formation of Fluorescent Metal (Au, Ag) Nanoclusters Capped in Bovine Serum Albumin Followed by Fluorescence and Spectroscopy. *J. Phys. Chem. C* **2011**, *115* (22), 10955−10963.
(44) Shang, L.; Azadfar, N.; Stockmar, F.; Send, W.; Trouillet, V.; Bruns, M.; Gerthsen, D.; Nienhaus, G. U. One-pot Synthesis of Near-infrared Fluorescent Gold Clusters for Cellular Fluorescence Lifetime Imaging. *Small* **2011**, *7* (18), 2614−2620.
(45) Luo, Z.; Yuan, X.; Yu, Y.; Zhang, Q.; Leong, D. T.; Lee, J. Y.; Xie, J. From Aggregation-induced Emission of Au(I)-thiolate Complexes to Ultrabright Au(0)@Au(I)-Thiolate Core-shell Nanoclusters. *J. Am. Chem. Soc.* **2012**, *134* (40), 16662−16670.
(46) Chan, P. H.; Ghosh, B.; Lai, H. Z.; Peng, H. L.; Mong, K. K. T.; Chen, Y. C. Photoluminescent Gold Nanoclusters as Sensing Probes for Uropathogenic Escherichia coli. *PLoS One* **2013**, *8* (3), e58064.
(47) Wang, H. H.; Lin, C. A. J.; Lee, C. H.; Lin, Y. C.; Tseng, Y. M.; Hsieh, C. L.; Chen, C. H.; Tsai, C. H.; Hsieh, C. T.; Shen, J. L.; Chan, W. H.; Chang, W. H.; Yeh, H. I. Fluorescent Gold Nanoclusters as a Biocompatible Marker for In Vitro and In Vivo Tracking of Endothelial Cells. *ACS Nano* **2011**, *5* (6), 4337−4344.
(48) Kunwar, P.; Hassinen, J.; Bautista, G.; Ras, R. H. A.; Toivonen, J. Direct Laser Writing of Photostable Fluorescent Silver Nanoclusters in Polymer Films. *ACS Nano* **2014**, *8* (11), 11165−11171.
(49) Liu, J.; Yu, M.; Zhou, C.; Yang, S.; Ning, X.; Zheng, J. Passive Tumor Targeting of Renal-Clearable Luminescent Gold Nanoparticles: Long Tumor Retention and Fast Normal Tissue Clearance. *J. Am. Chem. Soc.* **2013**, *135* (13), 4978−4981.
(50) Zhou, C.; Long, M.; Qin, Y.; Sun, X.; Zheng, J. Luminescent Gold Nanoparticles with Efficient Renal Clearance. *Angew. Chem., Int. Ed.* **2011**, *50* (14), 3168−3172.
(51) Zhang, X. D.; Chen, J.; Luo, Z.; Wu, D.; Shen, X.; Song, S. S.; Sun, Y. M.; Liu, P. X.; Zhao, J.; Huo, S.; Fan, S.; Fan, F.; Liang, X. J.; Xie, J. Enhanced Tumor Accumulation of Sub-2 nm Gold Nanoclusters for Cancer Radiation Therapy. *Adv. Healthcare Mater.* **2014**, *3* (1), 133−141.
(52) Fernandez, T. D.; Pearson, J. R.; Leal, M. P.; Torres, M. J.; Blanca, M.; Mayorga, C.; Le Guével, X. Intracellular Accumulation and Immunological Properties of Fluorescent Gold Nanoclusters in Human Dendritic Cells. *Biomaterials* **2015**, *43*, 1−12.
(53) Park, J.; Nam, J.; Won, N.; Jin, H.; Jung, S.; Jung, S.; Cho, S. H.; Kim, S. Compact and Stable Quantum Dots with Positive, Negative, or Zwitterionic Surface: Specific Cell Interactions and Non-specific Adsorptions by the Surface Charges. *Adv. Funct. Mater.* **2011**, *21* (9), 1558−1566.
(54) Dou, X.; Yuan, X.; Yao, Q.; Luo, Z.; Zheng, K.; Xie, J. Facile Synthesis of Water-soluble Au25−xAgx Nanoclusters protected by Mono- and Bi-thiolate ligands. *Chem. Commun.* **2014**, *50* (56), 7459−7462.
(55) Wu, Z.; Jin, R. On the Ligand's Role in the Fluorescence of Gold Nanoclusters. *Nano Lett.* **2010**, *10* (7), 2568−2573.
(56) Le Guevel, X. Recent Advances on the Synthesis of Metal Quantum Nanoclusters and their Application for Bioimaging. *IEEE J. Sel. Top. Quantum Electron.* **2014**, *20* (3), 1−12.
(57) Zhou, C.; Sun, C.; Yu, M.; Qin, Y.; Wang, J.; Kim, M.; Zheng, J. Luminescent Gold Nanoparticles with Mixed Valence States

DOI: 10.1021/acsami.5b06541
ACS Appl. Mater. Interfaces 2015, 7, 20945−20956

Generated from Dissociation of Polymeric Au(I) Thiolates. *J. Phys. Chem. C* **2010**, *114* (17), 7727−7732.
(58) Hong, Y.; Lam, J. W. Y.; Tang, B. Z. Aggregation-induced Emission. *Chem. Soc. Rev.* **2011**, *40* (11), 5361−5388.
(59) Jia, X.; Li, J.; Wang, E. Cu Nanoclusters with Aggregation Induced Emission Enhancement. *Small* **2013**, *9* (22), 3873−3879.
(60) Dunn, K. W.; Kamocka, M. M.; McDonald, J. H. A Practical Guide to Evaluating Colocalization in Biological Microscopy. *American Journal of Physiology - Cell Physiology* **2011**, *300* (4), C723−C742.
(61) Engering, A. J.; Cella, M.; Fluitsma, D.; Brockhaus, M.; Hoefsmit, E. C. M.; Lanzavecchia, A.; Pieters, J. The Mannose Receptor Functions as a High Capacity and Broad Specificity Antigen Receptor in Human Dendritic Cells. *Eur. J. Immunol.* **1997**, *27* (9), 2417−2425.
(62) Nam, H. Y.; Kwon, S. M.; Chung, H.; Lee, S. Y.; Kwon, S. H.; Jeon, H.; Kim, Y.; Park, J. H.; Kim, J.; Her, S.; Oh, Y. K.; Kwon, I. C.; Kim, K.; Jeong, S. Y. Cellular Uptake Mechanism and Intracellular Fate of Hydrophobically Modified Glycol Chitosan Nanoparticles. *J. Controlled Release* **2009**, *135* (3), 259−267.
(63) Khalil, I. A.; Kogure, K.; Akita, H.; Harashima, H. Uptake Pathways and Subsequent Intracellular Trafficking in Nonviral Gene Delivery. *Pharmacol. Rev.* **2006**, *58* (1), 32−45.
(64) Chen, C. L.; Hou, W. H.; Liu, I. H.; Hsiao, G.; Huang, S. S.; Huang, J. S. Inhibitors of Clathrin-dependent Endocytosis enhance TGFβ Signaling and Responses. *J. Cell Sci.* **2009**, *122* (11), 1863−1871.
(65) Macia, E.; Ehrlich, M.; Massol, R.; Boucrot, E.; Brunner, C.; Kirchhausen, T. Dynasore, a Cell-Permeable Inhibitor of Dynamin. *Dev. Cell* **2006**, *10* (6), 839−850.
(66) Shang, L.; Nienhaus, K.; Jiang, X.; Yang, L.; Landfester, K.; Mailänder, V.; Simmet, T.; Nienhaus, G. Nanoparticle Interactions with Live Cells: Quantitative Fluorescence Microscopy of Nanoparticle Size Effects. *Beilstein J. Nanotechnol.* **2014**, *5*, 2388−2397.
(67) Falcone, S.; Cocucci, E.; Podini, P.; Kirchhausen, T.; Clementi, E.; Meldolesi, J. Macropinocytosis: Regulated Coordination of Endocytic and Exocytic Membrane Traffic Events. *J. Cell Sci.* **2006**, *119* (22), 4758−4769.
(68) Zegers, M. M. P.; Zaal, K. J. M.; Van Ijzendoorn, S. C. D.; Klappe, K.; Hoekstra, D. Actin Filaments and Microtubules are Involved in Different Membrane Traffic Pathways that Transport Sphingolipids to the Apical Surface of Polarized HepG2 cells. *Mol. Biol. Cell* **1998**, *9* (7), 1939−1949.
(69) Zhang, L. W.; Bäumer, W.; Monteiro-Riviere, N. A. Cellular Uptake Mechanisms and Toxicity of Quantum Dots in Dendritic Cells. *Nanomedicine* **2011**, *6* (5), 777−791.
(70) dos Santos, T.; Varela, J.; Lynch, I.; Salvati, A.; Dawson, K. A. Effects of Transport Inhibitors on the Cellular Uptake of Carboxylated Polystyrene Nanoparticles in Different Cell Lines. *PLoS One* **2011**, *6* (9), e24438.

DOI: 10.1021/acsami.5b06541
ACS Appl. Mater. Interfaces 2015, 7, 20945−20956